

Dislocation plasticity and detwinning under thermal stresses in nanotwinned Ag thin films

Maya K. Kini*, Claudia Merola*, Benjamin Breitbach, Dennis Klapproth, Bastian Philipp†, Jean-Baptiste Molin, Christoph Kirchlechner‡, Gerhard Dehm

Max Planck Institut für Eisenforschung GmbH, Max-Planck-Strasse 1, 40237, Düsseldorf, Germany

*Current Address: Institute of Applied Physics, Technische Universität Wien, Vienna, Austria

†Current Address: AG der Dillinger Hüttenwerke, 66763 Dillingen, Germany

‡Current address: Institute of Applied Materials, Karlsruhe Institute of Technology, Hermann-von-Helmholtz-Platz 1, 76344 Germany

*Corresponding author

Email id: m.kini@mpie.de, kini.mayakatapadi@gmail.com

Abstract: Wafer curvature measurements reported in literature for polycrystalline (often textured) and epitaxial fcc metal thin films on hard substrates show a characteristic “signature” in the stress-temperature evolution for either type of films. While epitaxial films reveal characteristic elastic – ideal plastic deformation with no dislocation storage and highly repeatable cycles, polycrystalline films show considerable hardening upon cooling in addition to the relaxation by diffusional creep at elevated temperatures. In the present study, we study the deformation characteristics of an electron beam deposited epitaxial nanotwinned Ag on Si (111) substrate. The twin spacing λ of the nanotwinned Ag is controlled by suitable heat treatment and the “signature” thermomechanical deformation curves by wafer curvature measurements are recorded for twin spacings varying from 20 nm to 1 μm . Further, deformation is compared to other small scale deformation studies on fcc metals such as epitaxial bicrystal films, bicrystal micropillars containing a coherent twin boundary and nanotwinned micropillars.

Keywords: thin film plasticity, size effect, coherent twin boundaries, thermomechanical deformation, epitaxial nanotwinned fcc

1. Introduction

Thin film mechanics is an important area of mechanical metallurgy both from fundamental and application point of view. On the fundamental side, the area covers dislocation and diffusion based deformation processes at small length scales. On the application side, the mechanical strength of metallic films is an important aspect in the design of microelectronic devices that are versatile in the current age of electronics.

Deformation of metallic thin films is widely studied in literature [1-5]. Substrate curvature measurements using reflected laser beams combined with the Stoney equation [6] was one of the earliest and simplest methods suggested to measure residual stresses in thin films on substrate [1], [7]. The method is useful in measuring both growth and thermal stresses [8].

Thermal stresses originate from the mismatch in thermal expansion coefficient of the film (e.g. Al, Cu) and the substrate (e.g. Si or sapphire). On heating a metal film on substrate, higher thermal expansion coefficient of the metal leads to compressive stresses in the thin film. The film undergoes both elastic and plastic deformations based on the magnitude of the imposed thermal strains [9, 10]. Thermomechanical deformation of thin films on a substrate shows characteristic stress-strain curves depending on the film thickness, microstructure, texture, film-substrate interface and possible capping layer(s) [9-12]. Polycrystalline films, for example Cu on Si [13] deform by a combination of dislocation glide and diffusional creep with interesting features such as dislocation core spreading at the film- substrate interface [9, 14], “parallel glide dislocations” [15] and dislocation source limited strengthening [16]. In contrast, deformation of epitaxial films is characterized by the glide of threading dislocations leading to perfect elastic plastic stress-strain curves with very little strain hardening [9].

In coarse grained epitaxial Cu and Al thin films on c-sapphire with $\{111\}_{metal} \parallel (0001)_{sapphire}$, yield strength variation with thickness is in agreement with the Nix-Freund model for confined plasticity [1, 3, 9]. According to the model, yielding takes place when the work done by the applied stress ($\tau b h f(\varphi, \lambda)$) on threading dislocations is sufficient to deposit misfit dislocation segment (line energy $\sim \frac{\mu_{eff} b^2}{4\pi} \ln\left(\frac{\beta h}{b}\right)$) at the film-substrate interface, where τ is the resolved shear stress, b is the Burgers vector, h is the thickness of

the film, φ is the angle between the slip direction and the film normal, λ is the angle between the slip plane normal and the film normal, $\mu_{eff} = 2\mu_s\mu_f/(\mu_s + \mu_f)$ is the effective modulus for the film-substrate combination, β is a numerical constant related to the core cut off radius of a dislocation. The theory was supported by *in situ* TEM experiments [9], where gliding threading dislocations left behind misfit dislocations at the film – substrate interface during the cooling cycle. Similarly, during heating cycle dislocation loops expanded from these misfit dislocations, glided on inclined slip planes, cross slipped across coherent twin boundaries (CTBs) and disappeared at the film free surface. The dislocation density remained close to 10^{13} m^{-2} independent of temperature [17]. An almost constant dislocation density, absence of strain hardening [9] and a high degree of repeatability after a large number of cycles [18] indicated the escape of dislocations to the free surface due to a confined deforming volume. Although some theoretical models [19-21] suggested the interaction of misfit and threading dislocations leading to hardening, such observations were seldom observed in epitaxial films. Similarities can be drawn between the deformation of $\{111\}$ bicrystal epitaxial thin films containing predominantly incoherent $\Sigma 3 \{211\}$ twin boundaries (ITBs) [9] and micropillar compressions experiments on bicrystal micropillars containing coherent $\Sigma 3 \{111\}$ twin boundaries (CTB) [22]. Here we note that the state of stress is different (equibiaxial in thin films, uniaxial in pillar compression) leading to a lower Schmid factor 0.27 for wafer curvature measurements compared to 0.41 in micropillar compression. In addition, the total strain in thermally stressed thin films (usually $< 1\%$ in wafer curvature measurements) is much smaller compared to the micropillar compression experiments (where usually stress measurements are reliable at strains $> 2\%$). Despite these important differences, deformation shows several similarities: microstructural constraints (only CTBs and ITBs), limited number of dislocation sources [16, 23], escape of dislocations to the free surface forming slip steps, a constant dislocation density and a limited strain hardening during deformation hold good for both micropillar and thin film deformation. In addition, yield stress remains inversely proportional to characteristic length scale under both loading conditions [2].

Deformation of such bicrystals shows characteristic continuity of slip steps across the CTB indicating ideal or “cross-slip-like” slip transmission [24]. In a recent study, we extended the theory of ideal slip transmission to multiple closely (nm) spaced CTBs in nanotwinned Ag by

micropillar compression tests [25]. Epitaxial nanotwinned films [26] provide a special deformation geometry (only CTBs and ITBs) in contrast to polycrystalline nanotwinned films [27]. Findings of ideal slip transmission in bicrystal thin films (shown for Cu and Al [9]) and bicrystal / nanotwinned micropillars (shown for Ag [25]), naturally lead to a possibility of finding a similar deformation mode in epitaxial nanotwinned thin films. In the present study, we report thermomechanical deformation of epitaxial nanotwinned Ag thin film with varying twin spacing, supported on a Si substrate and compare results with previous micropillar compression results. Possibility of ideal slip transmission, size-scaling law, deformation twinning and detwinning are investigated and compared with literature.

2. Experimental procedure

2.1 Thin film deposition and characterization

Epitaxial Ag thin films on Si were deposited by electron beam evaporation in a Bestec PVD cluster (Bestec, Berlin, Germany). The Si $\langle 111 \rangle$ substrates (Si-Mat, Kaufering, Germany) were oxidized with $H_2SO_4:H_2O_2$ solution and etched by 30% aqueous HF. Deposition was carried out on etched wafers at room temperature at a deposition rate of $1\text{\AA}/s$ for the first 50 nm followed by a rate of $5\text{\AA}/s$ to a thickness of $2\text{ }\mu\text{m}$.

Deposited films were characterized for phase analysis and pole figure measurements in a Seifert diffractometer equipped with an ID3003 generator, a polycapillary beam optic, using Cu-K α radiation and a scintillation detector. The θ - 2θ overview measurements were carried out with a step size $\Delta 2\theta$ of 0.03° and a count time of 5s/step. The diffractometer was also equipped with a Huber 4 circle goniometer that enabled pole figure measurements with a ϕ range of $0 - 360^\circ$ about the rotation axis and a ψ range of $0 - 85^\circ$ about the tilt axis with a step size of 5° each. Pole figures were measured at 2θ values of 44.6° , 51.9° and 76.5° corresponding to $\{111\}$, $\{200\}$ and $\{220\}$ poles of Ag respectively. The texture data was analyzed using BEARTEX 2012x texture package software.

Further film microstructure was characterized and quantified by variant grain size d and twin spacing λ . The variant grain size was measured parallel to the film free surface - at 90 and 0°

to the Si flat (referred to as ‘horizontal’ and ‘vertical’ hereafter) and twin spacing perpendicular to the film surface. Films were tilted by 20° about the Si $\langle 1\bar{1}0 \rangle$ axis to maximize the channeling contrast and imaged with an annular Energy selective Backscatter (EsB®) in-lens detector or Quad-BSE detector in a Zeiss Gemini 500 SEM [28]. For measuring the twin spacing, a trench was made with a Zeiss Auriga® dual beam FIB / SEM using milling currents of 2nA and 120 - 240pA for the coarse and fine milling respectively. Further Electron Backscatter diffraction was carried out on a few samples in an EDAX TSL-OIM (version 6.0) data acquisition system attached to the Zeiss Auriga® dual beam FIB / SEM. Typical pole figures and microstructures of the as deposited film are shown in Fig. 1 and are explained in section 3.1.1 and 3.1.2.

2.2 Wafer curvature measurements

Equibiaxial state of stress in thin films was calculated using the Stoney equation [6],

$$\sigma_f = \frac{M_s h_s^2}{6h_f} \left(\frac{1}{R} \right) \quad (1)$$

where $M_s = 229.1$ GPa is the biaxial modulus of Si $\langle 111 \rangle$, $h_s = 275 \pm 25$ μm is the standard thickness of 2" Si substrates and $h_f = 2$ μm is the thickness of the film. The curvature $1/R$ of the Si substrate due to the residual stresses in the thin film was measured using a kSA-multibeam optical sensor (MOS) (k-Space Associates Inc., Dexter, USA) using a 3 x 4 array of laser spots (wavelength 660 nm) using the equation

$$\frac{1}{R} = \frac{\delta d \cos \alpha}{d \cdot 2L} \quad (2)$$

where d is the spot spacing of the incident Laser array, δd is the change in the spot spacing of the reflected array relative to the incident array, α is the angle between the incident beam and the sample normal and L is the distance between sample surface and the CCD camera. In the set up used for this study, L is much larger compared to the spot spacing d .

The system was calibrated using an optically flat mirror ($R \sim 20$ km) and a mirror with a known radius of curvature (10 m). A series of measurements were also carried out on as received 2" Si $\{111\}$ wafers from the same batch as those used for deposition.

Further, curvature measurements were also carried out on a number of pieces of e-beam evaporated 2 μm epitaxial Ag thin film on Si $\{111\}$. Plotting distributions of bare Si wafer as

well as Ag thin films enabled us to find the initial residual stress in epitaxial Ag films. Care was taken to align the flat of Si wafers (or $[1\bar{1}2]_{Si}$) parallel to the vertical axis and $[\bar{1}10]_{Si}$ along the horizontal axis of the wafer curvature set up.

2.3 Thermal stress evolution

Thermal strain $\Delta\alpha\Delta T$ leads to a thermoelastic deformation with a slope of $M_f\Delta\alpha$ where M_f is the biaxial modulus of the thin film and $\Delta\alpha$ is the difference in thermal expansion coefficient of the film and the substrate.

The wafer curvature set up had a pyrolytic BN heater in a vacuum chamber (vacuum level of $\sim 10^{-4}$ mBar at 500°C) connected to a Eurotherm controller that enabled multiple heating and cooling cycles at a precision of better than 1°C during entire thermal cycle. To minimize the temperature lag, the controlling thermocouple was fixed at the top of a dummy specimen (Si wafer piece) using Ta wires. A small drop of conductive Ag ink was placed at the thermocouple head.

Films were annealed at a temperature T_1 for 1 hour, followed by two subsequent thermal cycles to a temperature $T_2 = T_1 - 50^\circ\text{C}$ with no hold as shown in figure 2a. The first cycle to a higher temperature leads to a stable microstructure that remains unchanged during second and third thermal cycles. Overlapping of thermal cycling curves in the second and third cycle further validates this assumption. Yield stress σ_y and stress at 0.02% thermal strain (denoted as $\sigma_{0.02\%}$) were determined by fitting the elastic portion of the curve during the second and the third heating cycles from 30°C and cooling cycles from temperature of T_2 . The scaling of the 0.02% yield stress and the resolved shear stress were plotted with respect to the twin spacing λ and compared with micropillar compression results.

3. Results and Interpretation

3.1 Microstructure of nanotwinned epitaxial thin films

3.1.1 Orientation relationship with the substrate

The symmetric θ -2 θ measurements revealed strong $\{111\}$ and $\{222\}$ peaks with no other peaks. Corresponding X-Ray pole figure measurements showed strong epitaxial texture with

epitaxial and epitaxial twinned variants as shown in Fig 1a. Hereafter, these variants will be referred to as ‘variant 1’ and ‘variant 2’ respectively.

EBSD on the as deposited film shows double patterns as shown in the Fig. 3c (in contrast to the single crystal patterns in Fig. 3a and Fig. 3b) suggesting that the diffracting volumes of ‘variant 1’ and ‘variant 2’ are of the orders of the probe size, possibly tens of nm³. EBSD scans did not spatially / physically resolve variants in the as deposited state, although variants were “effectively” resolved [29]. The orientation relationship of Ag on Si substrate was found to be $\{111\}_{Ag} \parallel \{111\}_{Si}, \langle 1\bar{1}0 \rangle_{Ag} \parallel \langle 1\bar{1}0 \rangle_{Si}$ for variant 1 (epitaxial) and $\{111\}_{Ag} \parallel \{111\}_{Si}, \langle 10\bar{1} \rangle_{Ag} \parallel \langle 1\bar{1}0 \rangle_{Si}$ for variant 2 (epitaxial-twinned) respectively.

3.1.2 Twin spacing and variant grain size variation

Knowing the orientation of the variants with respect to the Si wafer enabled tilting to known angles leading to optimum channeling contrast between two variants [28]. A typical channeling contrast SEM image for the as deposited film with a thickness of 2 μm is shown in Fig 1b. Island morphology of thin film is clearly seen where variant 1 and 2 lamellae are arranged parallel to the film surface. Further image 1c shows the cross section of an as deposited film. Based on the Σ3 misorientation of the variants (from X ray pole figures and EBSD) with respect to each other and the grain boundary plane parallel to $\{111\}_{Ag}$ (in both variants, also parallel to $(111)_{Si}$), we infer that the film consists of multiple closely spaced coherent Σ3 (111) twin boundaries (CTBs) parallel to the substrate surface. Furthermore, the film possesses incoherent twin boundaries (ITBs) normal to the film / substrate interface. The planes of these ITBs are not well defined in the as deposited film. A few nanopores opening to the surface are seen in the plan view image 1b.

Figure 2 shows typical plan view and cross section channeling contrast images of films annealed to 300, 375 and 425°C respectively. A plot of an increase in variant spacing and twin spacing with increasing temperature is shown in Fig. 4. The in-plane variant size d slightly increases whereas the twin spacing λ increases by nearly two orders of magnitude. The only exception to the normal increasing trend with temperature is the sample annealed to 450°C (denoted as Ag34_WC11a in table 1), that was a sample from an edge of the Si wafer. Hence

we infer that the microstructure of films at the edge of the single side polished 2" Si substrate could differ from the typical behavior of the film taken from the center of the Si wafer.

In addition, nanopores were observed to be annihilated from the film even at the lowest annealing temperature of 200°C. At the highest annealing temperature of 450°C, ITBs formed clearly defined $\{112\}_{Ag}$ planes as shown by grain boundaries (thick black lines) in an EBSD-IPF map in Fig. 3e. Further, orientation spread was $< 2^\circ$ in the annealed samples as shown in Figs. 3d and f. The microstructure with variants 1 and 2 showed thermal stability up to a temperature of 450°C. However, exception to the thermal stability is occasional abnormal grain growth in some samples at random locations. In samples reported hereafter, abnormal grains covered $< 10\%$ area fraction. The crystallographic peculiarities of abnormal grain growth will be reported in a subsequent publication.

Interestingly, Ag grows epitaxially on Si to a thickness of up to 2 μm although the lattice mismatch strain between Si and Ag is 0.25, much higher than that expected for epitaxial growth. This high value of lattice strain is conventionally expected to lead to incoherent interfaces, practically at any film thickness. The critical thickness for misfit dislocation formation according to Matthews and Blackeslee [30] is 0.22 nm for Ag on Si. However, for Cu on MgO, with lattice mismatch of 0.14, an array of misfit dislocations is observed at the interface, with a mean spacing of 1.37 nm between dislocations [31]. Epitaxy of Ag on Si was earlier explained by lattice matching of three Si lattice parameters with four Ag lattice parameters [32], leading to a misfit strain of 0.0018. In analogy to Cu, it is possible that every fourth atomic plane is an edge dislocation at the interface- leading to an average dislocation spacing of 1.63 nm.

Epitaxy to a large film thickness in the present study is probably explained by easy nucleation of islands at surface steps and kinks on the $(111)_{Si}$ surface with large terraces [33] and the lowest surface energy for (111) oriented Ag. Formation of nanotwins as seen in the cross section is due to numerous re-nucleation events due to imposed rapid film growth conditions resulting from a high deposition rate. A low value of stacking fault energy of Ag [34] favors re-nucleation events. However, thicknesses greater than 2 μm lead to delamination when residual stresses in the system exceed the film- substrate interface strength.

3.2 Curvature of Si $\langle 111 \rangle$ wafers and initial stresses in epitaxial Ag thin films

Yield stress values reported in this study are from wafer curvature measurements. The measured initial stress values for as deposited 2 μm Ag films on Si are 240 ± 70 MPa (horizontal) and 270 ± 40 MPa (vertical) respectively. An inherent error in wafer curvature measurements due to initial curvature of the wafer, that often varies from wafer to wafer and can significantly affect findings. To account for initial residual stress in the thin film due to epitaxy the following equation could be used

$$\left(\frac{1}{R}\right)_{\text{effective}} = \left(\frac{1}{R}\right)_{\text{Ag on Si}\langle 111 \rangle} - \left(\frac{1}{R}\right)_{\text{Si}\langle 111 \rangle} \quad (3)$$

To account for the initial curvature of Si wafers, we cut bare 2" Si $\langle 111 \rangle$ wafers without any deposited film from the same batch used for deposition into rectangular pieces of $\sim 10 \times 10$ mm, followed by measurement of curvature on each of the cut wafer pieces. The cumulative probability distribution of the measured curvature values is shown in Fig. 5a. We see that the curvature measurements on bare Si can be fitted into a normal distribution with a mean value of $\left(\frac{1}{R}\right)_{\text{Si}\langle 111 \rangle} = -0.020 \pm 0.031$ (horizontal) and $\left(\frac{1}{R}\right)_{\text{Si}\langle 111 \rangle} = -0.027 \pm 0.032$ (vertical). These values translate into an initial stress of $\sim -40 \pm 50$ MPa (horizontal) and -40 ± 50 MPa (vertical) respectively for a 2 μm film according to the Stoney equation.

Subtraction of average stresses due to curvature of Si $\langle 111 \rangle$ from stresses measured in as deposited 2 μm Ag films lead to an initial tensile stress $\sigma_h \sim 280$ MPa (horizontal) and $\sigma_v \sim 310$ MPa (vertical). (Please note that subtraction of initial $(1/R)$ instead of initial stress leads to same results.) We used an initial stress value of 290 MPa, that is the average of horizontal and vertical stresses in our calculations. Widely separated distributions of Si $\langle 111 \rangle$ and Ag films as shown in Fig. 5b lead to an unambiguous determination of actual stresses during thermal cycles.

Calculated tensile stresses of $\sim +290$ MPa in the as deposited film are consistent with theoretical considerations considering difference in lattice parameters. Since $a_{\text{Ag}} \ll a_{\text{Si}}$, stresses in the film are expected to be tensile. However, considering a linear epitaxial strain of 0.25 with a biaxial modulus M_f of 170 GPa for Ag $\{111\}$ orientation (M_f is the biaxial

modulus of Ag for $\langle 111 \rangle$ orientation calculated using the equation $M_{(111)} = \frac{6C_{44}(C_{11}+2C_{12})}{C_{11}+2C_{12}+4C_{44}}$ [1] and the elastic constants [35-37].) leads to a theoretical residual stress of 40 GPa, a huge value clearly exceeding theoretical strength. However, the model based on $3a_{Si}$ with $4a_{Ag}$ leads to a compressive stress (-310 MPa), that is clearly not the case. We believe that the epitaxial tensile strain is accommodated by misfit dislocations at the film-substrate interface as mentioned earlier. In addition, under certain conditions there could be strain fields associated with partial dislocations at ITBs.

To account for the accuracy of the wafer curvature set up used, we also report curvature distributions on Si wafers other than 2" Si $\langle 111 \rangle$ in supplementary information. The distribution of curvature values of 2" Si $\langle 001 \rangle$ and 4" Si $\langle 001 \rangle$ compared to that of 2" Si $\langle 111 \rangle$ is shown in Fig. S1. As expected, the mean curvature is lower and distribution is narrower for 4" wafers that are thicker and stiffer. In addition, we note that for single side polished wafers, corner pieces lead to irregular laser spot arrays (unless the optic of kSA-MOS is adjusted) leading to unreliable values. Such pieces are avoided in most measurements. The 2" Si $\langle 001 \rangle$ wafers with diffusion barrier SiOx/ SiN (not used for the present study) lead to irregular spot arrays in most of the locations even at the center of the wafer.

3.3 Thermal stresses and deformation behavior with varying twin spacing

The as-deposited 2 μm epitaxial film with two growth variants was taken through thermal cycles to a range of temperatures between 200 and 450°C, listed in Tab. 1. The resulting thermal stress vs temperature curves along with cross sections in insets are shown in Fig. 6. The mean tensile stresses of the Ag film - Si(111) assembly in as deposited state was between 180 - 360 MPa (horizontal) and 280 – 330 MPa (vertical), the scatter being reasonable within the error limits of the curvature measurements. Stresses get compressive on heating due to the higher thermal expansion coefficient of the film compared to the substrate.

The slope to the elastic portion is given by

$$\frac{d\sigma_f}{dT} = M_f \Delta\alpha \quad (4)$$

where M_f is the biaxial modulus of Ag {111} and $\Delta\alpha = \alpha_f - \alpha_s$ is the difference in thermal expansion coefficients of the film and substrate. The temperature axis is linearly related to the thermal strain according to the relation $\varepsilon = \Delta\alpha (T - 30)$ where 30°C is the deposition

temperature. The value of $\Delta\alpha = \alpha_{Ag} - \alpha_{Si} = 14 \times 10^{-6}/K$ at 30°C [38]. Hence the linear portion in the σ - T curve is interpreted as elastically deforming region and any deviation from linear behavior is either plasticity or other processes leading to the residual stress relaxation due to annihilation of thermal stresses.

At lower temperatures ($\leq 250^\circ\text{C}$) (see e.g. first cycle in Figs. 6a), films undergo pure elastic deformation. Slight hysteresis seen at the beginning of heating and cooling cycles is attributed to the temperature lag in the system involving localized heating. Observation of pure elastic deformation suggests that the flow stress of the film remained greater than the thermal stress induced. From SEM images of cross sections shown in insets, we attribute this pure elastic deformation to “nanotwinned” behavior of thermomechanical deformation where there is no visible macroplasticity. The twin spacing in this region remains < 40 nm.

On heating to higher temperatures ($\geq 300^\circ\text{C}$), thermal relaxation processes begin at a temperature close to 300°C , subsequently the stresses in films get relatively tensile with increasing T (see first cycles in Fig. 6b and c). At the maximum temperature a hold segment of 60 minutes is included, which shows relaxation of the compressive stresses (Figs. 6a-c). Upon cooling, for films taken to temperatures $T \geq 400^\circ\text{C}$, the cooling cycle starts with an elastic deformation regime followed by ideal plasticity with negligible hardening as shown in Fig. 6b and c respectively. During subsequent heating / cooling cycles a nearly ideal elastic-plastic response is observed. Linear elasticity followed by ideal plasticity with no hardening is “signature” behavior reported in literature for epitaxial Cu and Al on c-sapphire with epitaxial and twinned variants and we refer the same as “epitaxial” behavior [9].

Interestingly when sufficient structural relaxation is allowed at higher temperatures, yield stresses at RT reduce compared to the as deposited film. This observation is similar to that in Al epitaxial films [39] and is explained in section 4.3.

3.4 Variation of 0.02% proof strength with twin spacing

To find the yield stress, the elastic portion of the cooling curve of second and third cycle is fitted to a linear function. Further, 0.02% flow stress is calculated by drawing a line parallel to the elastic portion, offset by a strain of 0.0002 (at a temperature of $\sim 74^\circ\text{C}$) as shown in Fig. 7a. A plot of 0.02% flow stress with the twin spacing is shown in Fig. 7b. The variation of 0.02% proof strength with inverse of twin spacing λ leads to a fitting exponents of 0.94 (horizontal)

and 0.77 (vertical) for heating cycles, that are close to the value reported for Cu thin films (~ 0.7) [2] and higher compared to epitaxial Al (~ 0.5). The exponents of 0.02% flow stress deduced from the cooling cycles at temperatures of $(T_2 - 44)^\circ\text{C}$ are found to be 0.32 (horizontal) and 0.42 (vertical) respectively. Here flow stresses in heating cycles are expected to be more accurate as all measurements are carried out at a constant temperature, hence independent of temperature effects on the flow stress.

Twin spacing was selected as the sole characteristic length scale that is much smaller than the variant grain size for all specimens except the highest λ of $1\ \mu\text{m}$, where the variant size d is comparable to λ . In Fig. 8, we show the comparison of yield stress and the resolved shear stress for yielding in wafer curvature measurements to our recent micropillar compression results on similar films [25]. To calculate the Schmid factor for biaxial state of stress, we found the resolved shear stress in the coordinate system of one of the 6 equivalent slip systems from the available stress state in the film coordinate system. Film coordinate system was taken as a combination of vectors $[\bar{1}10]$, $[1\bar{1}2]$ and $[111]$. Two vectors in slip system correspond to the slip plane normal $[\bar{1}\bar{1}\bar{1}]$ and the slip direction $[110]$ respectively. All vectors were normalized and the stress σ_{12}' (shear stress along the slip direction) was found to be $0.27\ \sigma$, leading to a Schmid factor of 0.27. In contrast, the Schmid factor for the geometry used in our pillar compression experiments was 0.41 [25].

We note that the reported wafer curvature derived stress values are lower estimates for the nanotwinned Ag with $\lambda < 40\ \text{nm}$ (yield stress is higher than applied stress, samples deformed elastically in the selected temperature range). At $\lambda > 100\ \text{nm}$, the flow stresses (at 0.02% strain) in the wafer curvature measurements are up to a factor of 2 - 4 smaller compared to micropillar compression (flow stress at 2% strain).

4. Discussion

4.1 Thermoelastic deformation

Slopes to the elastic portion for varying twin spacing are listed in Tables 2 and 3 and plotted in Fig. 9a. The theoretical value for Ag $\{111\}$ on Si $\{111\}$ is calculated as 2.7 MPa/K at room temperature and increases to 3.3 MPa/K at 500°C as shown in Fig. 9b [35-38]. Especially for the heating cycles at temperatures ($< 100^\circ\text{C}$), the calculated thermoelastic slope varies between 2.0 and 2.6 MPa/K, that is close to the theoretical value of 2.7 MPa/K. In cooling

cycles, the slope increases from ~ 2.4 MPa/K for $\lambda < 40$ nm to 3.8 MPa/K for the single/bicrystal film. The increase in observed slope at higher temperatures can only be partially attributed to the increase in the theoretical value of $\Delta\alpha$. Similarly, the change in M_s and M_f values probably influence our results.

Here we exclude the possibility of error in temperature measurements based on the following observations: firstly, temperatures on both controlling thermocouple (on dummy Si wafer) and secondary thermocouple (directly on the BN heating stage) were much lower than the expected temperature for the observed value from Fig. 9b (that is $\sim 800^\circ\text{C}$ for 3.8 MPa/K [38]). Secondly, if there is error in temperature due to highly localized heating, we expect temperature of the sample to be lower than the heating stage due to heat dissipation. Thirdly, experiments on polycrystalline films of other metallic systems in the same set up heated to same temperatures do not show any such discrepancy. From the observations listed above we infer that the observed increase in thermoelastic slope is typical to epitaxial Ag on Si.

The nanopores present at the surface could lead to reduction in the modulus if present in significant fraction, but annihilation of nanopores at 200°C does not drastically change the slope. Further the slope is not due to the formation of secondary phases with a higher modulus. Si and Ag form a eutectic system [40] where there is negligible solid solubility up to the eutectic temperature. Formation of secondary phases such as silicides were not observed in any of the cross sections. The diffusion of impurities (for example oxygen) into the film due to a higher solubility at higher temperatures could lead to a higher slope. However, since the heating slopes remain unaffected and curves remain highly repeatable, we exclude this as a major cause.

The apparent increase in the elastic slope beyond the theoretical value may only be attributed to two reasons: first the temperature dependence of constants α_{Si} , α_{Ag} , M_s and M_f . Second, the local elastic deformation of the Silicon substrate at higher temperatures due to a reduced stiffness. A strong film-substrate interface possibly leads to such local deformation of the substrate. We note that this is clearly in contrast to stiffer substrates such as c-sapphire.

4.2 Comparison of resolved shear stresses for yielding in uniaxial and biaxial deformation

Firstly, we observe no significant strain hardening in σ - ϵ curves across the range of λ from 40 nm to $1\ \mu\text{m}$. We note that the elastic deformation is followed by an ideal plastic deformation

for all twin spacings. The typical curves shown in Fig. 6 remain “signature” of thermomechanical deformation for epitaxial Ag with a given twin spacing. Curves for larger twin spacings show a strong resemblance to epitaxial Al and Cu on c-sapphire [9] and are considerably different compared to the polycrystalline films [13]. Neither diffusion creep during heating cycle, nor strain hardening regime at the low temperature end of the cooling cycle is observed in any of the $\sim 2 \mu\text{m}$ nanotwinned films in a total of 33 experiments. In addition, very small spread in misorientation in EBSD ($< 2^\circ$) imply a negligible geometrically necessary dislocation density in annealed films. Hence deformation is similar to epitaxial single crystal/bicrystal films [9] and nanotwinned micropillars [25], indicating a perfect slip transmission across CTB/ ITBs.

It is notable that the resolved shear stresses in thin film deformation are lower by a factor of 2 – 4 compared to pillar compression results on the same material processed under similar conditions. We also note that the limited data available for comparison of resolved shear stress for the epitaxial Cu films and microtensile/ compression tests on single crystal Cu micropillars [2, 41] also shows a factor of ~ 1.5 difference between datasets. Here, the flow stresses in micropillar compression studies are reliable at strain levels of $> 2\%$ compared to the thermal straining of thin films where flow stresses at much lower strain levels can be measured accurately and reproducibly. In some micropillar compression studies an upper estimate of 5% strain was taken [42] to ensure reported flow stress in the stable deformation regime. Considering the strain differences in wafer curvature studies and micropillar compression, we believe that a factor of 2 – 4 for the resolved shear stresses is acceptable. However, in Fig. S2 we also show a plot of flow stress for the onset of plastic deformation in micropillar compression (which is possibly not an accurate representation of the deformation but serves comparison) compared to the 0.02% flow stress in thermal straining of films, that shows negligible difference between two sets of data. However, the CRSS in wafer curvature measurements is still a factor of 2 lower compared to micropillar compression onset yield stress.

In literature, lower CRSS in thin film deformation is attributed to the Bauschinger effect due to dislocations at the film- substrate interface, the density of which is expected to increase with increasing thermal strain [43, 44]. In some cases [44], the Bauschinger effect leads to apparent negative yield stresses. In the present study, negative yield stress (for example, yield

at an apparent tensile stress under compressive loading) was only due to erroneous measurements [Tabs. 2 and 3] (samples from the edge) and no negative yielding is observed. However, Bauschinger effect due to interfacial dislocations leading to a lower yield stress cannot be ruled out. Based on the lattice mismatch we expect a high interfacial dislocation density at Si – Ag interface at all temperatures. As mentioned earlier, a lattice mismatch of 0.25 for Ag on Si theoretically leads to one dislocation for every fourth Ag plane, with a dislocation spacing of ~ 1.63 nm. In fact, in MeV ion channeling studies [45], a dislocation density near the interface in ~ 250 nm {111} epitaxial Ag thin film on Si (111) was found to be one order of magnitude higher compared to the bulk of the film.

A comparison with theoretical models shows a much weaker twin spacing (λ) dependence of the yield stress compared to the film thickness (h) dependence in Nix- Freund model [1] for the glide of threading dislocations (Fig. 8a). In addition, the twin spacing (λ) dependence of CRSS is also weaker compared to the film thickness (h) dependence in the source model by von Blanckenhagen [16] (Fig. 8b). Although we don't attempt to quantify the power law exponent due to limited datapoints and lower estimate $\sigma_{0.02}$ for $\lambda < 40$ nm, results are broadly consistent with the micropillar compression study, where twin spacing dependence showed a weaker dependence [25] compared to the pillar diameter dependence [46].

The deformation in micropillar compression and continuity of slip steps across multiple CTBs was explained by a Friedel–Escaig type cross-slip behavior (see Fig. 10) through twin boundaries for specific screw dislocations where their lines only locally increase in curvature due to constriction at the CTB forming a perfect transmitting screw dislocation [25]. In the present study, we note that slip traces were visible in both variants at the unmodified free surface of deformed thin films as shown in Fig. 10b and c. Slip traces were parallel to $\langle 110 \rangle$ type of directions that are also the traces of {112} ITBs on the {111} free surface, making them easy to be identified in high resolution SEM topography images. Observations of slip traces in films with multiple CTBs across the cross section serve as an indirect evidence for dislocation plasticity during thermal straining. However, a direct observation of such a mechanism requires *in situ* TEM or *in situ* ECCI studies in future.

The resolved shear stresses in this study are close to the values for constriction of partial dislocations at the CTB, that are expected to be in the range of 12 – 55 MPa at room temperature and reduce slightly at higher temperatures [25].

4.3 Detwinning under thermal stresses

During first heating (annealing) cycle, at temperatures between 300 and 400°C, films show a slight non-linearity or deviation from linear elastic portion. Conventionally the change in trend from increasingly compressive to tensile stress is attributed to the onset of diffusional processes [13], that also lead to defect annihilation in the first heating cycle. However, in the present study the majority of defects are twin boundaries (CTBs and ITBs). There was no evidence of diffusional creep (observed in polycrystalline Ag films but not in epitaxial films, see Fig. S3b) or hillock formation due to grain boundary diffusion in epitaxial Ag films. Annihilation of nanopores takes place even on annealing to temperatures of < 200°C with no macroscopic indication in the σ - T curves. In addition, all annealed samples show a smoother film surface removing irregularities due to growth islands, the trend that is reverse as expected to the hillock formation.

Examination of the microstructures annealed to temperatures > 200°C shows an increase in twin spacing and the variant sizes with increasing T as discussed earlier. Hence the compressive stress relaxation above 300°C during first heating cycle is predominantly due to detwinning that progressively reduces the yield stress of the film.

Note that the detwinning is observed even in cases with no macroscopic indication in the stress – temperature (strain) curves. Compressive stress for the onset of macroscopic observation is 300 to 360 MPa and a macroscopic thermal strain of close to 0.004 in all cases. To qualitatively assess temperature effects in wafer curvature measurements we compare twin spacing of a sample taken through 2 thermal cycles to 300 and 325°C with no hold time and the sample held at 300, 325°C for 1 hour each. From the Table 1, it is very clear that the twin spacing λ remains the same for samples with no holding time and 1 hour holding time at a given temperature. Results indicate that the detwinning is possibly an athermal process where kinetics was fast enough that holding time had very little influence. However, this observation is again qualitative given the limited datapoints. However, decoupling of stress and temperature effects on detwinning requires experimental methods other than wafer curvature techniques – hence are beyond the scope of the present study.

Detwinning starts at lower stresses compared to the plastic yielding confirming the reports of a lower CRSS for the former process [47]. In literature, detwinning is reported to be due to the migration of incoherent twin boundaries (ITBs) by a collective glide of dislocations at

ITBs due to shear stresses acting on CTB planes [48]. It is notable that the detwinning can take place despite no macroscopic strain [49] (effective Burgers vector of zero for a combination of dislocations). In the present study, despite a zero resolved shear stress on CTB planes (that are parallel to the film – substrate interface) extensive detwinning takes place. Earlier studies revealed local stress inhomogeneities in thin films by Laue diffraction [50]. Such stress inhomogeneities can be explained by the local relaxation of stresses at the micron and sub-micron scale –for example, by operation of individual dislocation sources. Especially at grain boundaries local stress inhomogeneities are foreseen which can lead to unexpected shear stresses deviating from the continuum prediction. Drawing similarities, deformation by dislocation plasticity could lead to stress inhomogeneities especially at the ITBs leading to extensive partial dislocation glide on CTB planes and their migration under thermomechanical stresses. In addition, interaction of gliding full dislocations with ITB dislocations could lead to detwinning [51].

We also note the absence of considerable deformation twinning on inclined $\{111\}$ planes despite a low stacking fault energy of Ag [34] which is due to a low plastic strain of <0.006 . However, we acknowledge that this is an overall observation; locally thin twin lamellas could be present which will be addressed through the ECCI [52] and TEM studies in future.

5. Summary and Conclusions

In the present study, we study the thermomechanical deformation of epitaxial nanotwinned Ag with varying twin spacing λ under the biaxial state of stress. The study is complementary to the recent report on micropillar compression on nanotwinned epitaxial Ag with varying twin spacing [25].

- Epitaxial nanotwinned Ag films on chemically etched Si (111) wafer were deposited by electron-beam evaporation. Despite a large epitaxial strain of 0.25 Ag grows epitaxially on Si, at least up to a film thickness of 2 μm .
- The twin spacing λ perpendicular to the film increases from ~ 20 nm to 1 μm on annealing, whereas the change in variant spacing d parallel to the film remains marginal.

- Epitaxial nanotwinned Ag on Si, with $\lambda > 40$ nm shows elastic - ideal plastic thermomechanical deformation during wafer curvature measurements. In addition, films with $\lambda < 40$ nm show pure elastic deformation due to limited accessible temperature (and therefore strain) range.
- CRSS for wafer curvature measurements is a factor of 2 – 4 lower both in heating and cooling compared to micropillar compression. The observation is partly attributed to the small strains in wafer curvature experiments compared to micropillar compression testing. In addition, a high area density of interfacial misfit dislocations at the film-substrate interface due to large lattice mismatch may also affect dislocation glide leading to a difference in yield stress between the freestanding micropillars and films supported on the substrate.
- The twin spacing λ dependence of the biaxial strength is much weaker compared to the film thickness dependence calculated from theoretical models [1, 16].
- Detwinning occurs at much lower stresses compared to plastic yielding confirming a much lower CRSS for the former process.

Acknowledgements:

Technical assistance on FIB-SEMs by Volker Kree and Leon Christiansen, on substrate preparation by Angelika Bobrowski and on electronics by Ivan Gonzalez and Michael Koelling is gratefully acknowledged. MKK acknowledges the fellowship of the Max-Planck society during initial phase of the project. GD acknowledges financial support by the ERC Advanced Grant GB-CORRELATE (Grant No. 787446).

References

- [1] W.D. Nix, Mechanical-Properties of Thin-Films, *Metall Trans A* 20(11) (1989) 2217-2245.
- [2] G. Dehm, Miniaturized single-crystalline fcc metals deformed in tension: New insights in size-dependent plasticity, *Prog Mater Sci* 54(6) (2009) 664-688.
- [3] R.P. Vinci, J.J. Vlassak, Mechanical behavior of thin films, *Annu Rev Mater Sci* 26 (1996) 431-462.
- [4] R.S. Fertig, S.P. Baker, Simulation of dislocations and strength in thin films: A review, *Prog Mater Sci* 54(6) (2009) 874-908.
- [5] G. Abadias, E. Chason, J. Keckes, M. Sebastiani, G.B. Thompson, E. Barthel, G.L. Doll, C.E. Murray, C.H. Stoessel, L. Martinu, Review Article: Stress in thin films and coatings: Current status, challenges, and prospects, *J Vac Sci Technol A* 36(2) (2018).
- [6] G.G. Stoney, The tension of metallic films deposited by electrolysis, *P R Soc Lond a-Conta* 82(553) (1909) 172-175.
- [7] P.A. Flinn, D.S. Gardner, W.D. Nix, Measurement and Interpretation of Stress in Aluminum-Based Metallization as a Function of Thermal History, *Ieee T Electron Dev* 34(3) (1987) 689-699.
- [8] G.C.A.M. Janssen, M.M. Abdalla, F. van Keulen, B.R. Pujada, B. van Venrooy, Celebrating the 100th anniversary of the Stoney equation for film stress: Developments from polycrystalline steel strips to single crystal silicon wafers, *Thin Solid Films* 517(6) (2009) 1858-1867.
- [9] G. Dehm, T.J. Balk, H. Edongue, E. Arzt, Small-scale plasticity in thin Cu and Al films, *Microelectron Eng* 70(2-4) (2003) 412-424.
- [10] A.A. Taylor, S.H. Oh, G. Dehm, Microplasticity phenomena in thermomechanically strained nickel thin films, *J Mater Sci* 45(14) (2010) 3874-3881.

- [11] M.J. Kobrinsky, G. Dehm, C.V. Thompson, E. Arzt, Effects of thickness on the characteristic length scale of dislocation plasticity in Ag thin films, *Acta Mater* 49(17) (2001) 3597-3607.
- [12] S.P. Baker, A. Kretschmann, E. Arzt, Thermomechanical behavior of different texture components in Cu thin films, *Acta Mater* 49(12) (2001) 2145-2160.
- [13] D. Weiss, H. Gao, E. Arzt, Constrained diffusional creep in UHV-produced copper thin films, *Acta Mater* 49(13) (2001) 2395-2403.
- [14] G. Dehm, E. Arzt, In situ transmission electron microscopy study of dislocations in a polycrystalline Cu thin film constrained by a substrate, *Appl Phys Lett* 77(8) (2000) 1126-1128.
- [15] T.J. Balk, G. Dehm, E. Arzt, Parallel glide: unexpected dislocation motion parallel to the substrate in ultrathin copper films, *Acta Mater* 51(15) (2003) 4471-4485.
- [16] B. von Blanckenhagen, P. Gumbsch, E. Arzt, Dislocation sources and the flow stress of polycrystalline thin metal films, *Phil Mag Lett* 83(1) (2003) 1-8.
- [17] E. Arzt, Overview no. 130 - Size effects in materials due to microstructural and dimensional constraints: A comparative review, *Acta Mater* 46(16) (1998) 5611-5626.
- [18] W. Heinz, R. Pippan, G. Dehm, Investigation of the fatigue behavior of Al thin films with different microstructure, *Mat Sci Eng a-Struct* 527(29-30) (2010) 7757-7763.
- [19] L.B. Freund, The Stability of a Dislocation Threading a Strained Layer on a Substrate, *J Appl Mech-T Asme* 54(3) (1987) 553-557.
- [20] W.D. Nix, Yielding and strain hardening of thin metal films on substrates, *Scripta Mater* 39(4-5) (1998) 545-554.
- [21] P. Pant, K.W. Schwarz, S.P. Baker, Dislocation interactions in thin FCC metal films, *Acta Mater* 51(11) (2003) 3243-3258.

- [22] P.J. Imrich, C. Kirchlechner, C. Motz, G. Dehm, Differences in deformation behavior of bicrystalline Cu micropillars containing a twin boundary or a large-angle grain boundary, *Acta Mater* 73 (2014) 240-250.
- [23] S.W. Lee, W.D. Nix, Size dependence of the yield strength of fcc and bcc metallic micropillars with diameters of a few micrometers, *Philos Mag* 92(10) (2012) 1238-1260.
- [24] N.V. Malyar, B. Grabowski, G. Dehm, C. Kirchlechner, Dislocation slip transmission through a coherent $\Sigma 3\{111\}$ copper twin boundary: Strain rate sensitivity, activation volume and strength distribution function, *Acta Mater* 161 (2018) 412-419.
- [25] M.K. Kini, G. Dehm, C. Kirchlechner, Size dependent strength, slip transfer and slip compatibility in nanotwinned silver, *Acta Mater* 184 (2020) 120-131.
- [26] D. Bufford, H. Wang, X. Zhang, High strength, epitaxial nanotwinned Ag films, *Acta Mater* 59(1) (2011) 93-101.
- [27] L. Lu, Y.F. Shen, X.H. Chen, L.H. Qian, K. Lu, Ultrahigh strength and high electrical conductivity in copper, *Science* 304(5669) (2004) 422-426.
- [28] Y. Yahiro, K. Kaneko, T. Fujita, W.J. Moon, Z. Horita, Crystallographic orientation contrast associated with Ga⁺ ion channelling for Fe and Cu in focused ion beam method, *J Electron Microsc* 53(5) (2004) 571-576.
- [29] S. Zaefferer, G. Habler, Scanning electron microscopy and electron backscatter diffraction, *Emu Notes Mineralog* 16 (2017) 37-95.
- [30] J.W. Matthews, A.E. Blakeslee, Defects in Epitaxial Multilayers .1. Misfit Dislocations, *J Cryst Growth* 27(Dec) (1974) 118-125.
- [31] S. Cazottes, Z.L. Zhang, R. Daniel, J.S. Chawla, D. Gall, G. Dehm, Structural characterization of a Cu/MgO(001) interface using C-S-corrected HRTEM, *Thin Solid Films* 519(5) (2010) 1662-1667.

- [32] F.K. Legoues, M. Liehr, M. Renier, W. Krakow, Microstructure of Epitaxial Ag/Si(111) and Ag/Si(100) Interfaces, *Philos Mag B* 57(2) (1988) 179-189.
- [33] P. Wynblatt, D. Chatain, Two-dimensional versus three-dimensional constraints in hetero-epitaxy/orientation relationships, *J Mater Sci* 52(16) (2017) 9630-9639.
- [34] D.J. Cockayne, M.L. Jenkins, I.L.F. Ray, Measurement of Stacking-Fault Energies of Pure Face-Centred Cubic Metals, *Philos Mag* 24(192) (1971) 1383-&.
- [35] S.N. Biswas, P. Vantklooster, N.J. Trappeniers, Effect of Pressure on the Elastic-Constants of Noble-Metals from 196-Degrees-C to +25-Degrees-C and up to 2500-Bar .2. Silver and Gold, *Physica B & C* 103(2-3) (1981) 235-246.
- [36] P. Mohazzabi, Temperature-Dependence of the Elastic-Constants of Copper, Gold and Silver, *Journal of Physics and Chemistry of Solids* 46(1) (1985) 147-150.
- [37] J.R. Neighbours, G.A. Alers, Elastic Constants of Silver and Gold, *Physical Review* 111(3) (1958) 707-712.
- [38] L.B.S. Freund, S., *Thin Film Materials: Stress, Defect Formation and Surface Evolution*, Cambridge University Press 2004.
- [39] G. Dehm, B.J. Inkson, T. Wagner, Growth and microstructural stability of epitaxial Al films on (0001) alpha-Al₂O₃ substrates, *Acta Mater* 50(20) (2002) 5021-5032.
- [40] R.W.G. Olesinski, A.B.; Abbaschian, G.J., The Ag-Si (Silver-Silicon) System, *Bulletin of Alloy Phase Diagrams* 10(6) (1989) 635-640.
- [41] N.V. Malyar, J.S. Micha, G. Dehm, C. Kirchlechner, Size effect in bi-crystalline micropillars with a penetrable high angle grain boundary, *Acta Mater* 129 (2017) 312-320.
- [42] C.A. Volkert, E.T. Lilleodden, Size effects in the deformation of sub-micron Au columns, *Philos Mag* 86(33-35) (2006) 5567-5579.

- [43] Y. Xiang, J.J. Vlassak, Bauschinger effect in thin metal films, *Scripta Mater* 53(2) (2005) 177-182.
- [44] S.P. Baker, R.M. Keller-Flaig, J.B. Shu, Bauschinger effect and anomalous thermomechanical deformation induced by oxygen in passivated thin Cu films on substrates, *Acta Mater* 51(10) (2003) 3019-3036.
- [45] G.A. Smith, K.H. Park, G.C. Wang, T.M. Lu, W.M. Gibson, Defect Analysis of Epitaxial Ag Films on Silicon by MeV Ion Channeling, *Surf Sci* 233(1-2) (1990) 115-122.
- [46] S. Buzzi, M. Dietiker, K. Kunze, R. Spolenak, J.F. Löffler, Deformation behavior of silver submicrometer-pillars prepared by nanoimprinting, *Philos Mag* 89(10) (2009) 869-884.
- [47] Z.S. You, X.Y. Li, L.J. Gui, Q.H. Lu, T. Zhu, H.J. Gao, L. Lu, Plastic anisotropy and associated deformation mechanisms in nanotwinned metals, *Acta Mater* 61(1) (2013) 217-227.
- [48] J. Wang, N. Li, O. Anderoglu, X. Zhang, A. Misra, J.Y. Huang, J.P. Hirth, Detwinning mechanisms for growth twins in face-centered cubic metals, *Acta Mater* 58(6) (2010) 2262-2270.
- [49] Y.D. Wang, W.J. Liu, L. Lu, Y. Ren, Z.H. Nie, J. Almer, S. Cheng, Y.F. Shen, L.A. Zuo, P.K. Liaw, K. Lu, Low Temperature Deformation Detwinning-A Reverse Mode of Twinning, *Adv Eng Mater* 12(9) (2010) 906-911.
- [50] N. Tamura, A.A. MacDowell, R. Spolenak, B.C. Valek, J.C. Bravman, W.L. Brown, R.S. Celestre, H.A. Padmore, B.W. Batterman, J.R. Patel, Scanning X-ray microdiffraction with submicrometer white beam for strain/stress and orientation mapping in thin films, *J Synchrotron Radiat* 10 (2003) 137-143.
- [51] N. Li, J. Wang, X. Zhang, A. Misra, In-situ TEM Study of Dislocation-Twin Boundaries Interaction in Nanotwinned Cu Films, *Jom-U* 63(9) (2011) 62-U62.

[52] I. Gutierrez-Urrutia, S. Zaefferer, D. Raabe, Coupling of Electron Channeling with EBSD: Toward the Quantitative Characterization of Deformation Structures in the SEM, Jom-Us 65(9) (2013) 1229-1236.

Figures with captions and Tables

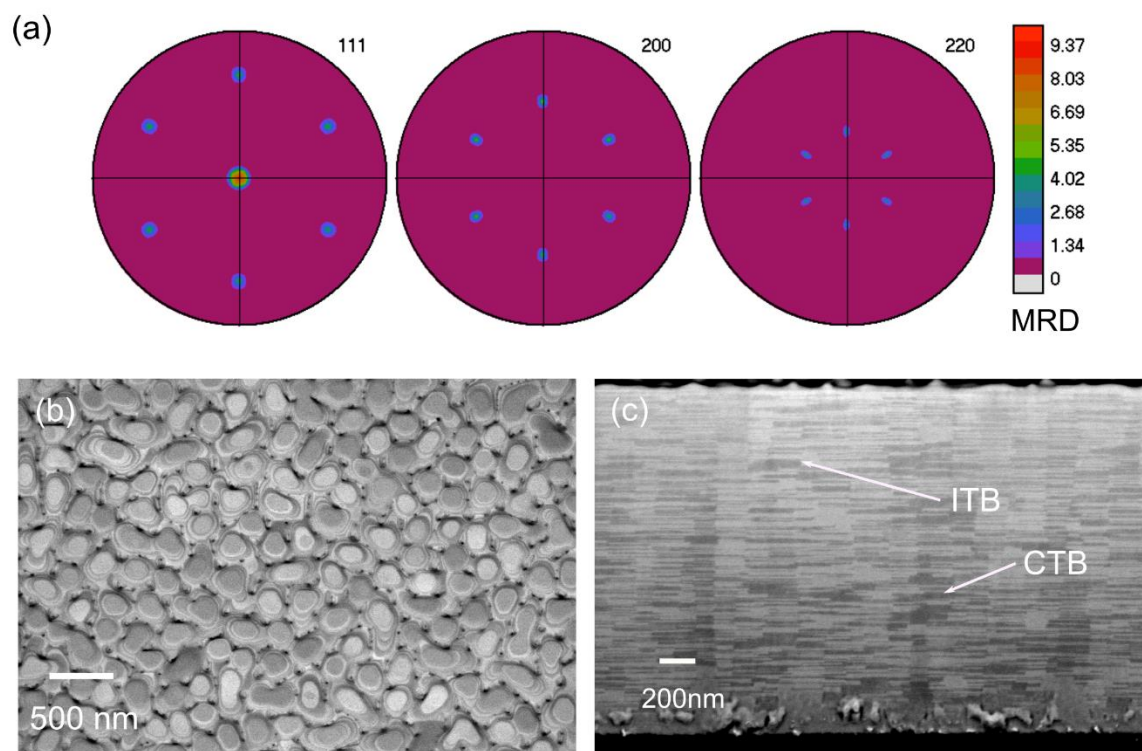


Fig. 1: (a) $\{111\}_{Ag}$, $\{200\}_{Ag}$ and $\{220\}_{Ag}$ X-ray pole figures; (b) electron channeling contrast SEM image of the film surface revealing some surface topography and a few nanopores. (c) Cross section of an as deposited 2 μm thick Ag film on Si(111); grey contrast differences in (c) reveal the two twin variants detected in (a).

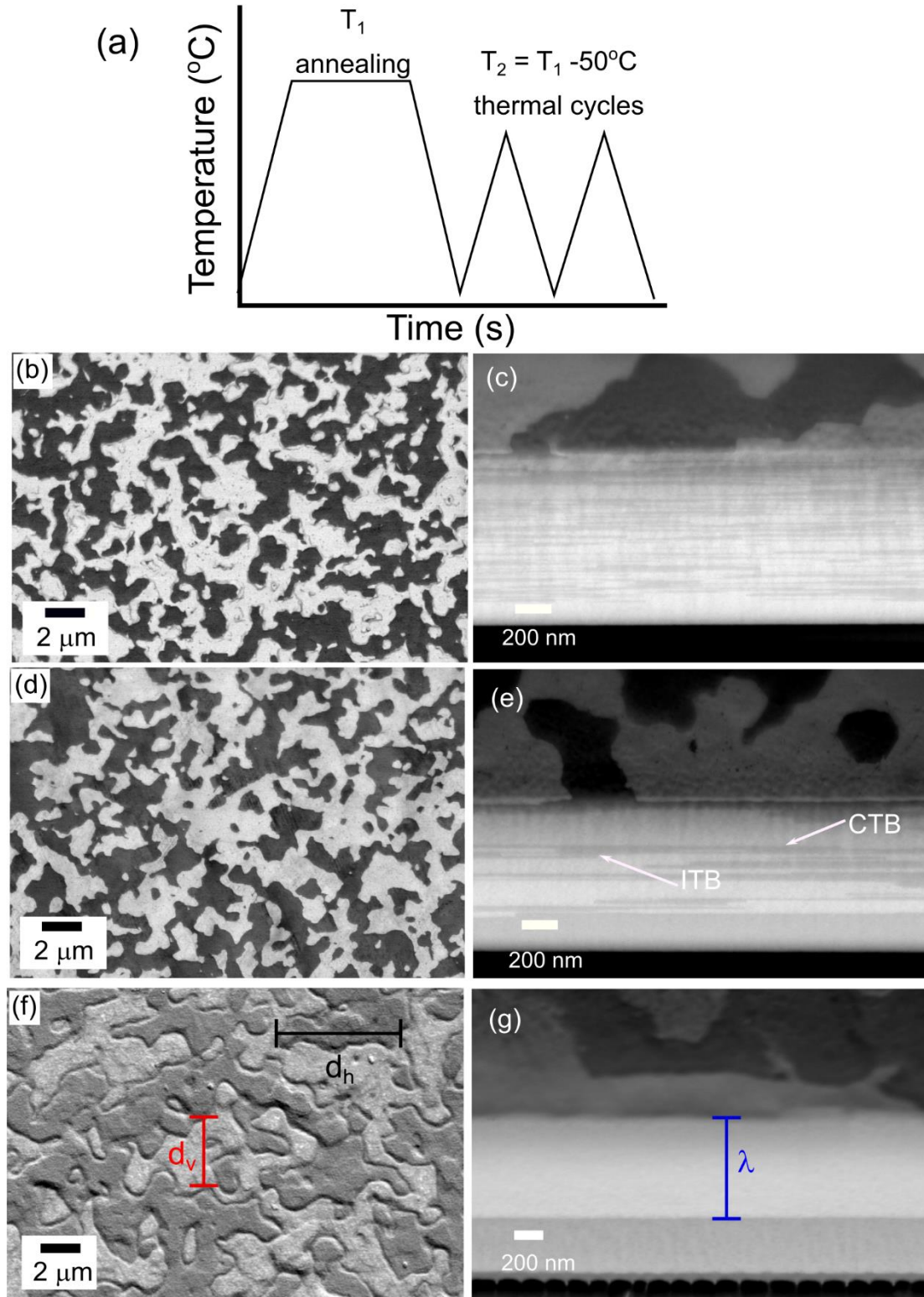


Fig. 2: (a) A schematic of a typical annealing, thermal cycling schedule. (b), (d), (f) are the plan view channeling contrast SEM images and (c), (e), (g) are cross section images of samples annealed to 300, 375 and 425°C respectively.

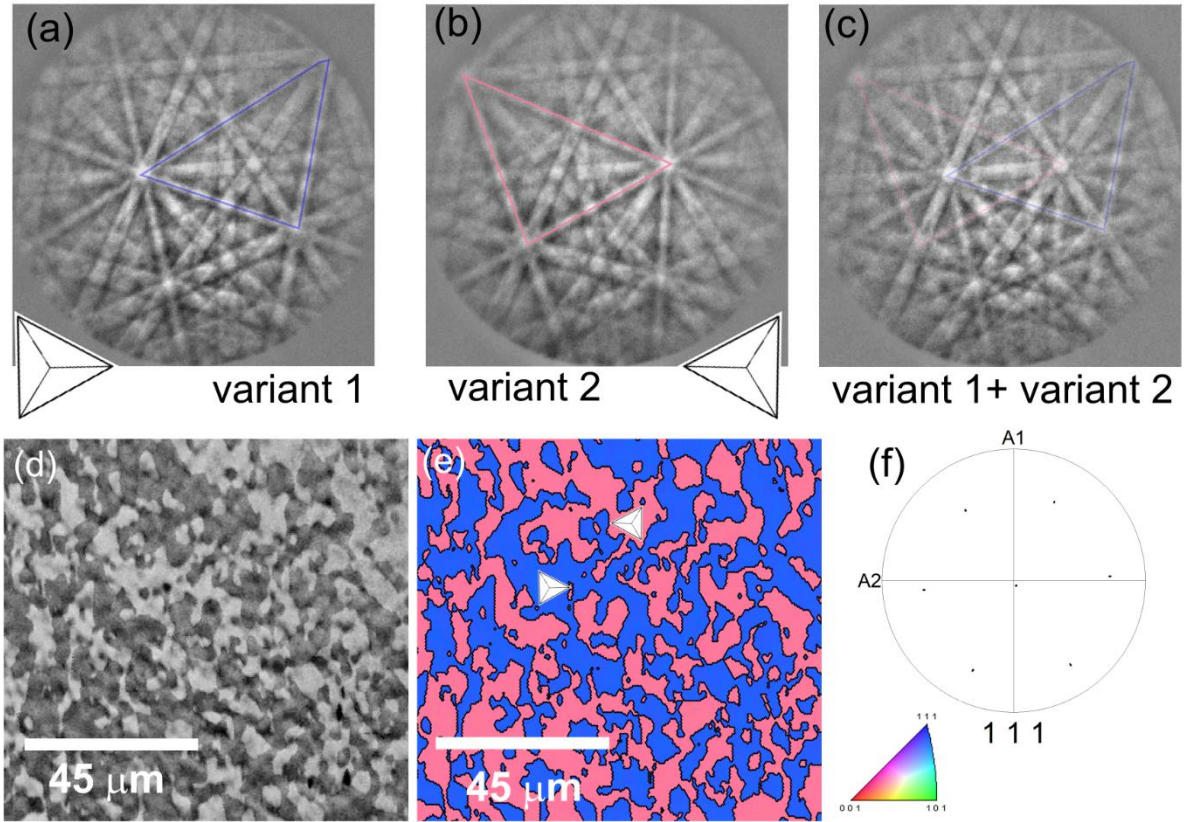


Fig. 3: Kikuchi pattern under Electron backscatter diffraction (EBSD) conditions for (a) variant 1 (b) variant 2 (c) “double pattern” or the overlapped Kikuchi patterns from both variants in the as deposited film – with closely spaced variant 1 and 2 along the sample normal. For reference, Thompsons double tetrahedron schematics for variant 1 and 2 are shown below the corresponding Kikuchi patterns. In addition, to make the mirror symmetry clearer, a reference triangle is drawn on Kikuchi patterns (no physical meaning – colored lines are visual aids). (d) is the image quality (IQ) map and (e) the inverse pole figure (IPF) map along the direction $[943, 0, 334]$ in the sample coordinate system - corresponding to the inclined $\{111\}_{Ag}$ in the variant 1, (f) the $\{111\}_{Ag}$ pole figure (PF) from EBSD data on an annealed sample.

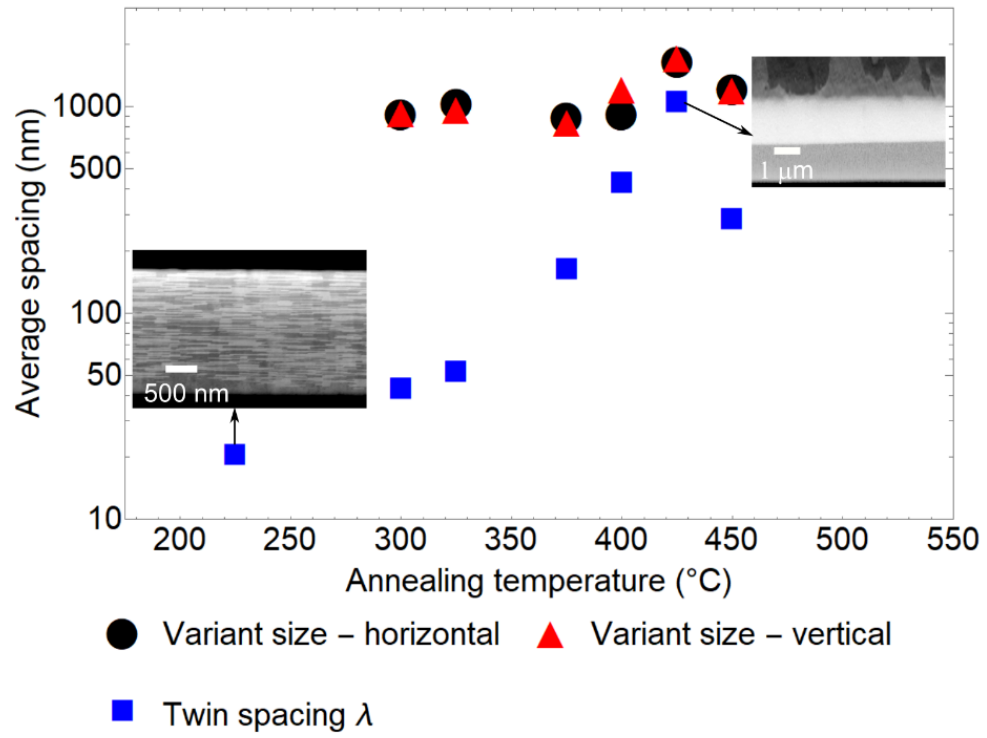


Fig. 4: Increase in twin spacing λ and the variant size d (horizontal and vertical) with annealing temperature.

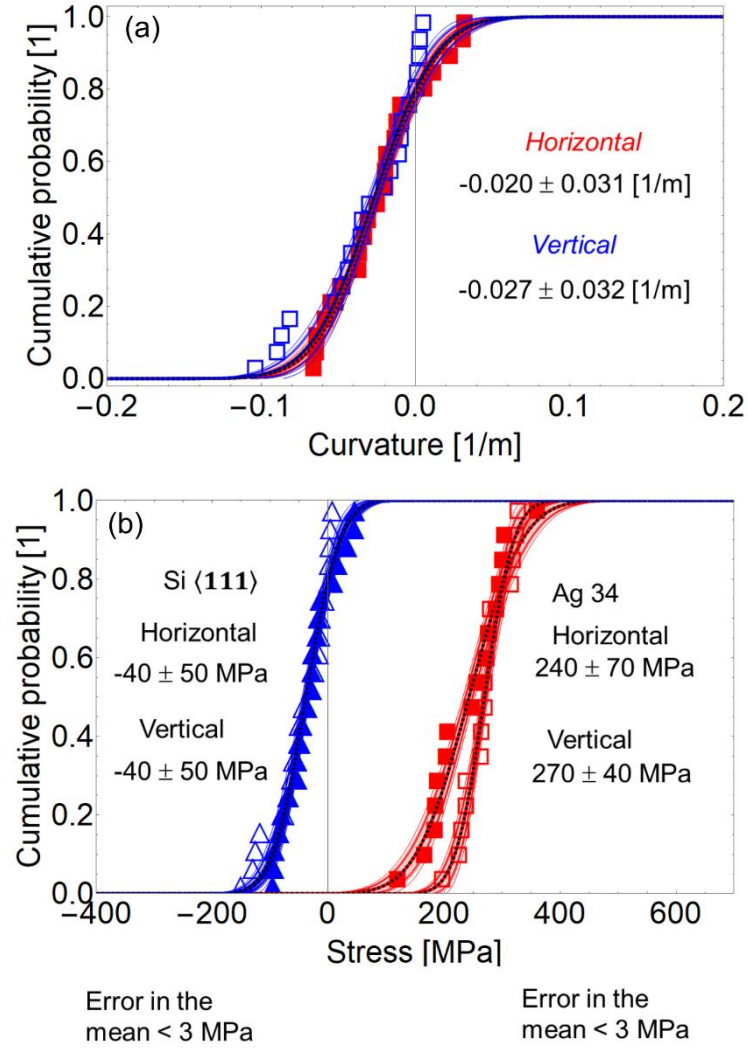


Fig. 5: Cumulative probability distribution (CDF) fitted with normal distribution for (a) horizontal (parallel to $\langle 110 \rangle_{Si}$) and vertical (parallel to $\langle 112 \rangle_{Si}$) curvature of Si (111) wafers. (b) Cumulative probability distribution of the resulting stresses due to initial curvature of Si wafer and measured stresses for as deposited 2 μm nanotwinned Ag films.

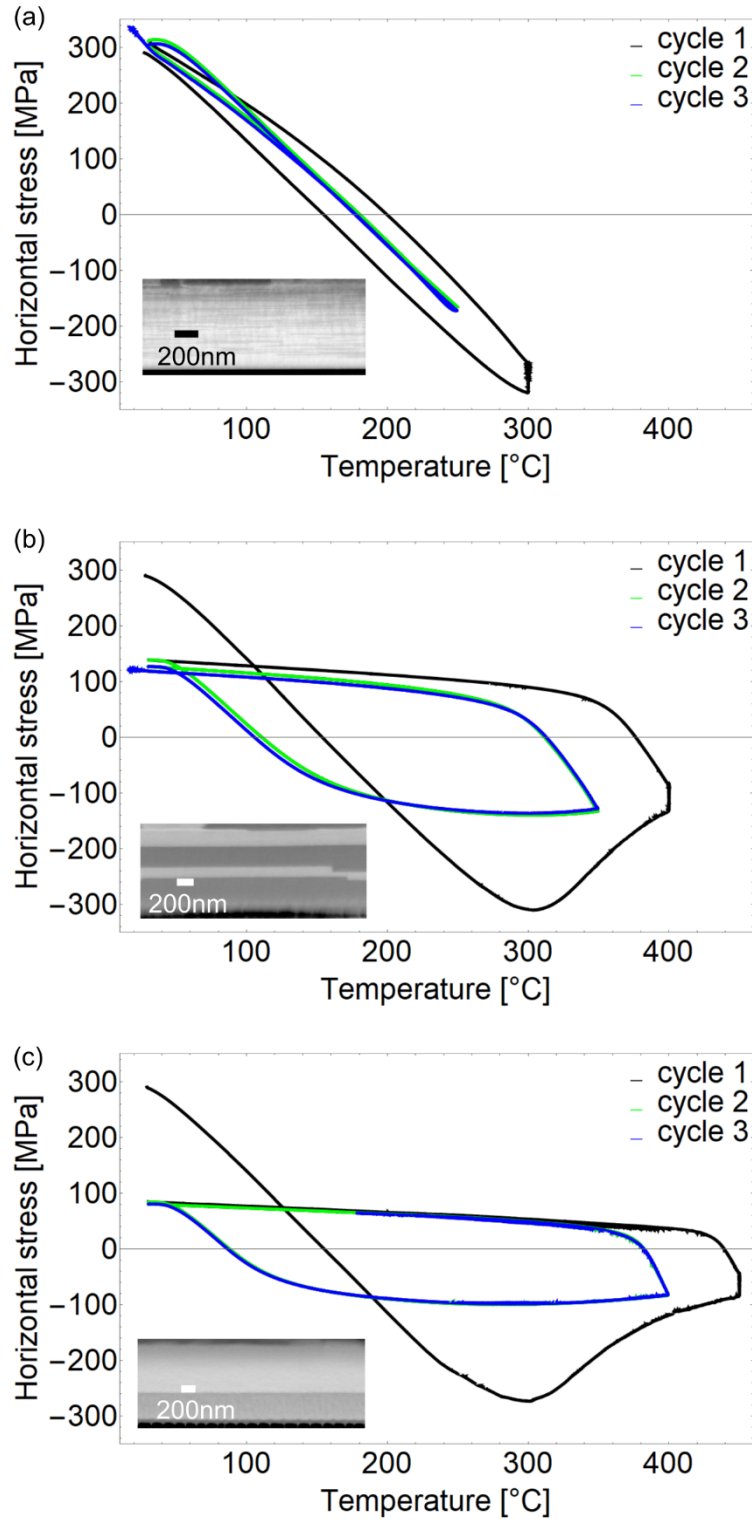


Fig. 6: Representative thermomechanical deformation curves of 2 μm thick nanotwinned Ag films with varying twin spacing λ . The insets show the typical microstructure at the end of third cycle. Cycle 1 (black) is the annealing cycle, cycle 2 (green) and cycle 3 (blue) (both to a lower temperature) are thermomechanical deformation cycles.

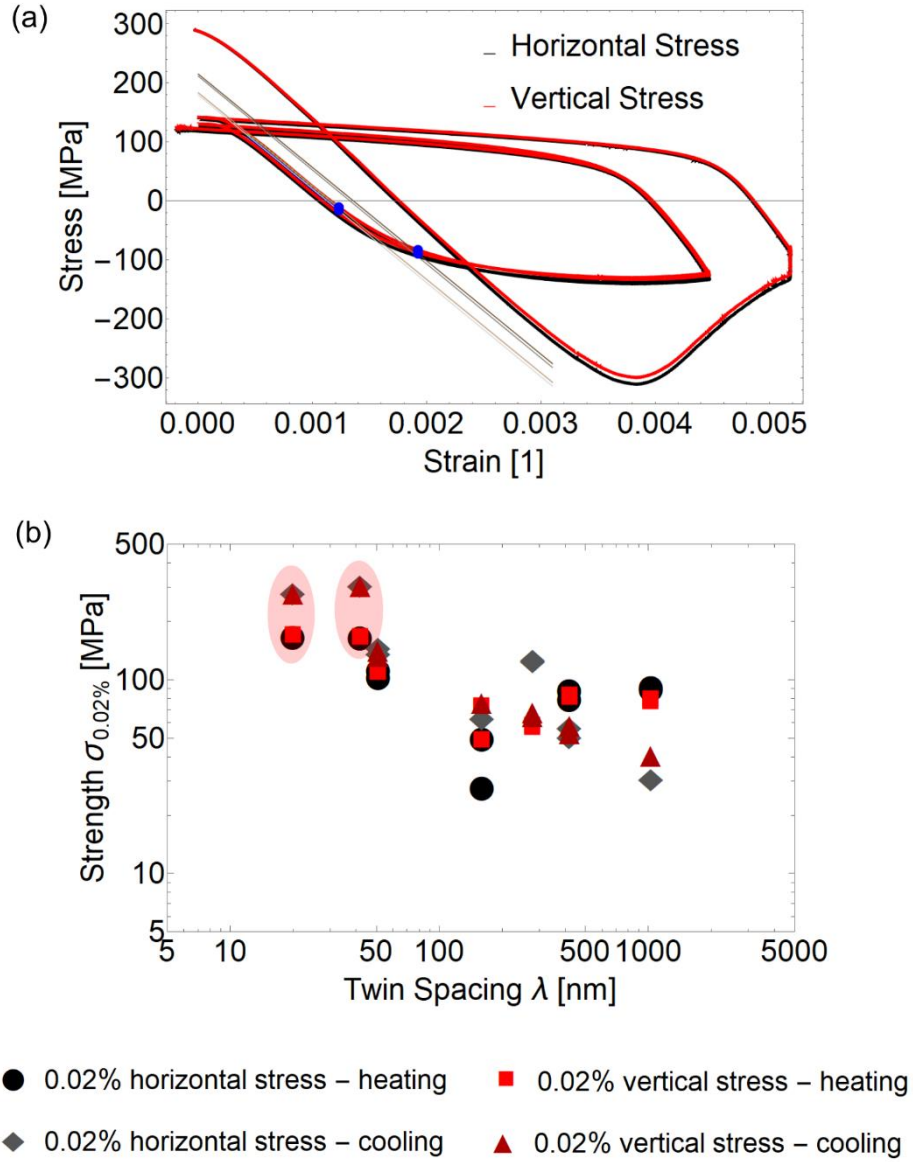


Fig. 7: (a) Linear fitting to the elastic portion – to determine elastic slope, yield stress and 0.02% proof stress (b) 0.02% proof stress variation with varying λ . Marked data points in (b) are lower estimates of the flow stress.

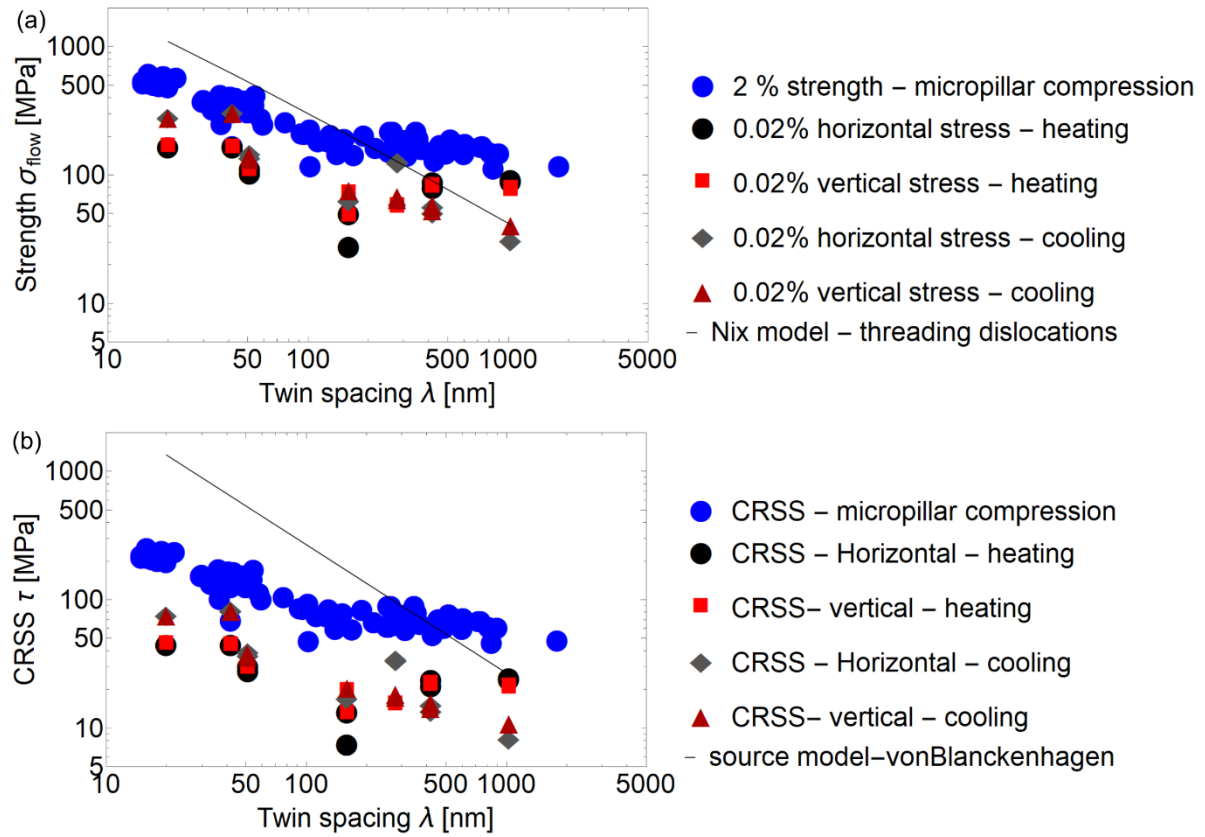


Fig. 8: (a) Variation of 0.02% proof strength and (b) resolved shear stress (considering a Schmid factor of 0.27 for the thermally induced equi-biaxial stresses) for varying twin spacing λ compared with micropillar compression tests on similar samples [25] and theoretical thin film models [1, 16].

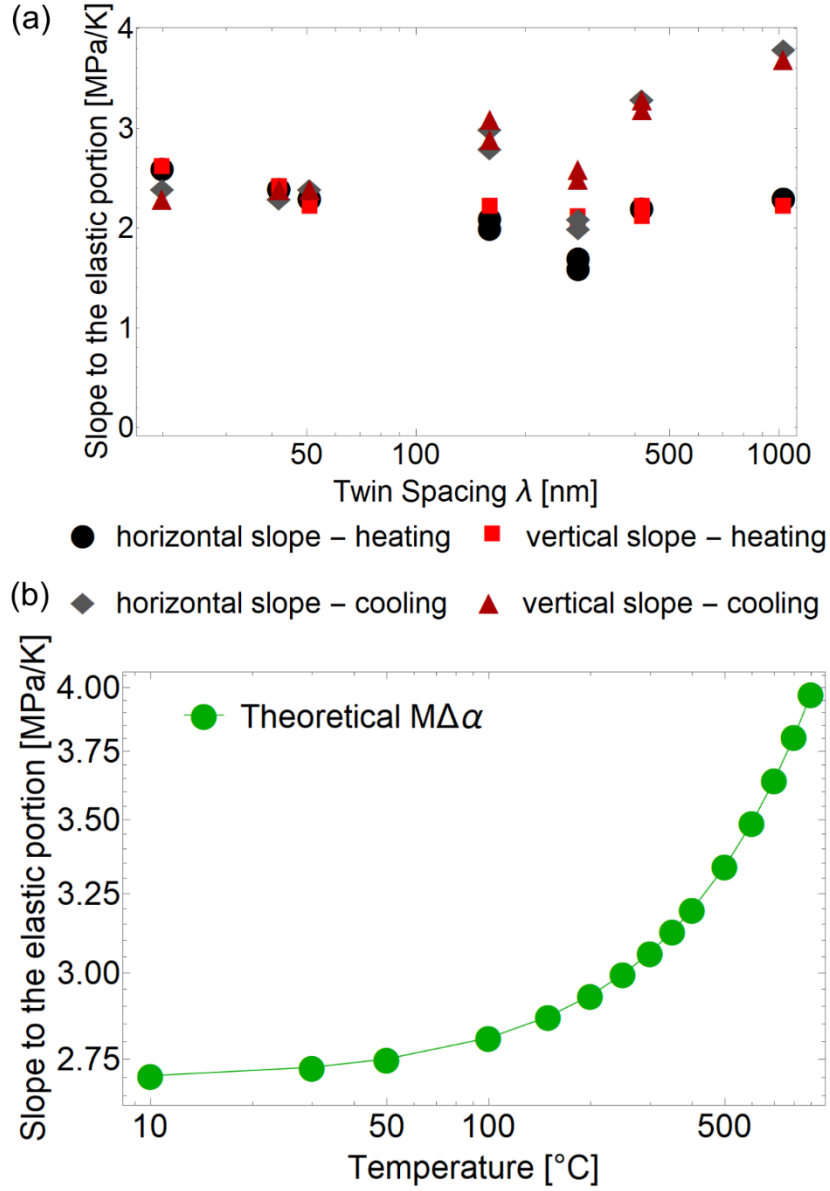


Fig 9: (a) Elastic slopes $M_f \Delta\alpha$ (MPa/K) for heating and cooling cycles (b) the theoretical values of $M_f \Delta\alpha = M_f (\alpha_{Ag} - \alpha_{Si})$, with varying temperature. The value increases with increasing temperature due to the linear temperature dependent terms in α_{Ag} and α_{Si} . The values of these constants are taken from [37].

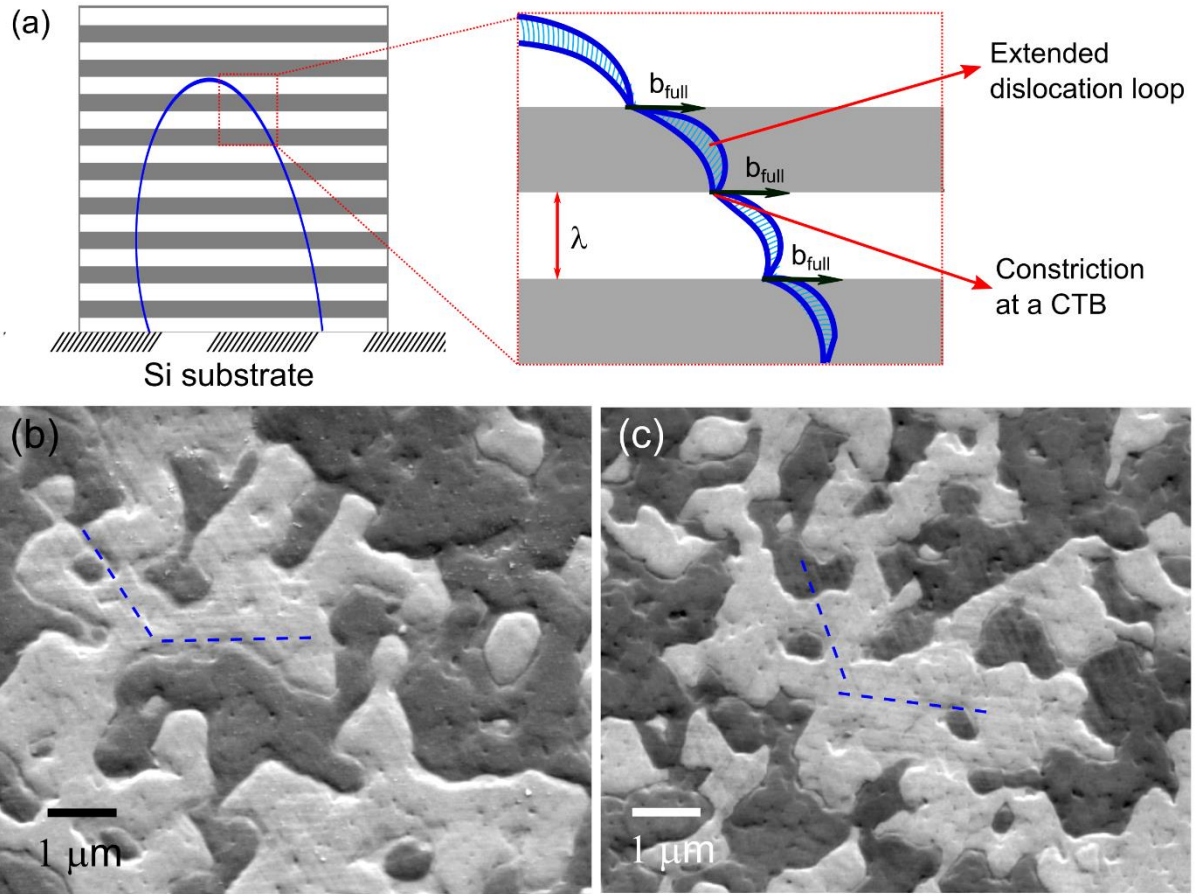


Fig 10: (a) A schematic of a possible dislocation configuration due to biaxial thermomechanical deformation in nanotwinned Ag. Dislocation loops are expected to form by the expansion of threading interfacial dislocations at the film – substrate interface [9], further extended dislocations are expected to form constrictions at each CTB, followed by cross-slip like slip transmission across the CTB. (b) and (c) slip traces observed in thermally cycled samples. Blue dotted lines are visual aids parallel to slip traces.

Table 1: List of annealing and thermal cycling temperatures with variant grain size along horizontal and vertical axes and the twin spacing. All samples except Ag34_WC11a and Ag34_WC14 were taken from the center of the Si wafer. The Ag34_WC11a and Ag34_WC14 were taken from the edge.

Reference sample No.	Temperature T_1 (°C)	Temperature T_2 (°C)	Variant grain size d_h (nm)	Variant grain size d_v (nm)	Variant grain size d_{avg} (nm)	Twin spacing λ (nm)
Ag34_WC10	225	225	-	-	-	~20
Ag34_WC13	300 (250	930 ± 3	950 ± 2	940 ± 4	42 ± 1
Ag34_WC17	325	275	1050 ± 2	990 ± 3	1020 ± 4	52 ± 1
Ag34_WC14	375	325	900 ± 2	850 ± 3	870 ± 4	170 ± 2
Ag34_WC11a	450	400	1240 ± 4	1220 ± 3	1230 ± 5	310 ± 4
Ag34_WC12	400	350	930 ± 1	1230 ± 3	1070 ± 3	440 ± 18
Ag34_WC16	425	375	1670 ± 3	1750 ± 7	1710 ± 7	1160 ± 48
Ag34_WC4	300 (2 cycles, no hold)					37 ± 1
Ag34_WC9	325 (2 cycles, no hold)	325 (one cycle)				52 ± 2

Table 2: Variation of the elastic slopes, yield stress, 0.02% flow stress upon (a) heating and (b) cooling as a function of twin spacing. Two values in the same column correspond to two successive thermal cycles. Samples from edge of the 2" Si wafer ($\lambda = 170\text{nm}$, 310nm) show erroneous stress values (indicated by *) and are not plotted in Fig. 7.

(a) Heating cycle

Twin spacing λ (nm)	Heating					
	Elastic slope (MPa/K)		Yield stress (MPa)		0.02% proof stress (MPa)	
	Horizontal	vertical	Horizontal	vertical	Horizontal	vertical
~ 20	2.6,2.6	2.6,2.5	>-190	>-190	>-190	>-190
42 ± 1	2.4,2.4	2.4,2.4	> -170	> -170	> -170	> -170
52 ± 1	2.3,2.3	2.2,2.2	-10,-10	-10,-10	-113,-104	-108,-108
170 ± 2	2.1,2.0	2.2,2.2	56*, 27*	43*, 11*	-28,-50	-42, -72
310 ± 4	1.6,1.7	2.1,2.0	21*, 21*	74*, 73*	56*, 57*	14*, 14*
440 ± 18	2.2,2.2	2.1,2.2	-15, -13	-10, -28	-89,-80	-82,-80
1160 ± 48	2.2,2.2	2.1,2.2	-24, -36	-12, -24	-92, -90	-78, -76

(b) Cooling cycle

Twin spacing λ (nm)	Cooling					
	Elastic slope (MPa/K)		Yield stress (MPa)		0.02% proof stress (MPa)	
	Horizontal	vertical	Horizontal	vertical	Horizontal	vertical
~ 20	2.3, 2.4	2.3,2.4	>280	>280	>280	>280
42 ± 1	2.3,2.3	2.4,2.4	>300	>300	>300	>300
52 ± 1	2.4,2.4	2.4,2.4	48, 39	51, 43	147, 138	145, 135
170 ± 2	2.8,3.0	2.9,3.2	6, -28*	-14, -50	128, 126	69, 66
310 ± 4	2.1,2.1	2.5,2.6	110, 96	33, 16	160, 160	99, 96
440 ± 18	3.3,3.3	3.3,3.2	11, 18	15, 22	57, 51	59, 54
1160 ± 48	3.8	3.7	-16 *	-6, *	31	41

Dislocation plasticity and detwinning under thermal stresses in nanotwinned Ag thin films

Maya K. Kini*, Claudia Merola*, Benjamin Breitbach, Dennis Klapproth, Bastian Philippit, Jean-Baptiste Molin, Christoph Kirchlechner‡, Gerhard Dehm

Email id: m.kini@mpie.de, kini.mayakatapadi@gmail.com

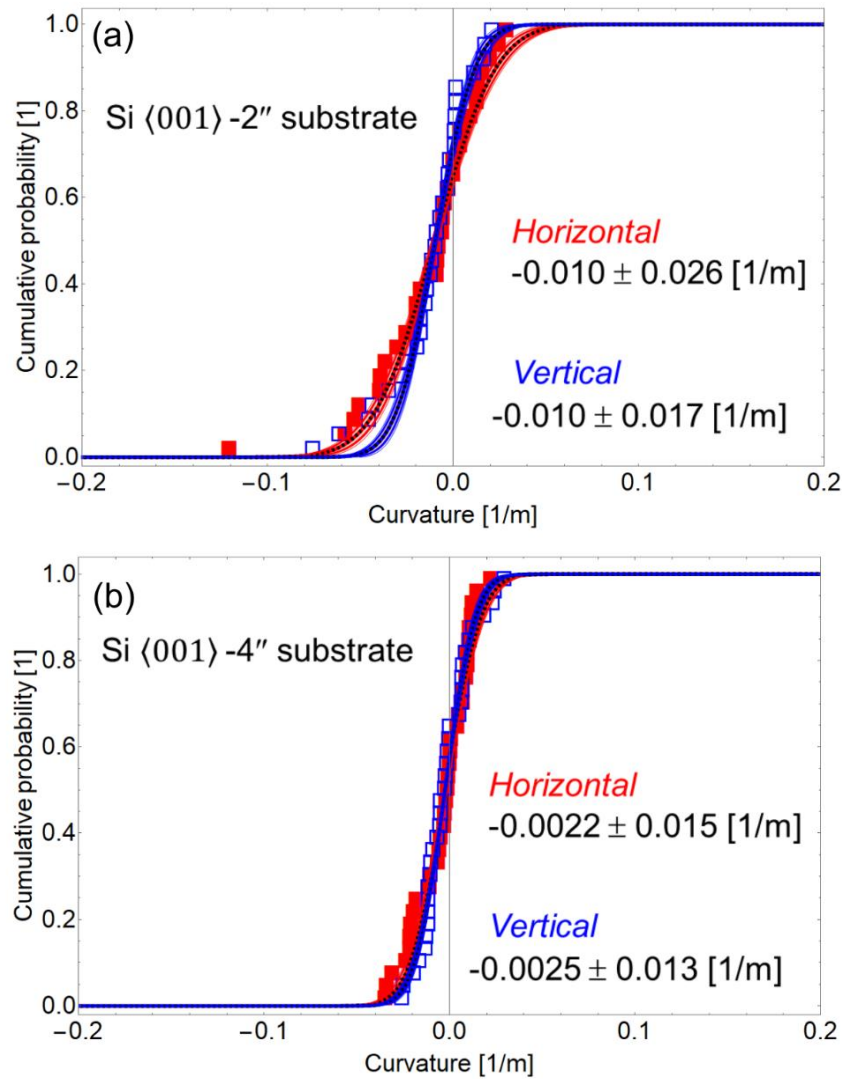


Fig S1: the cumulative probability distribution (CDF) of the curvature $1/R$ calculated from the measured laser spot spacing relative to a flat mirror. the (a) Si $\langle 001 \rangle$ – 2" substrate (b) Si $\langle 001 \rangle$ – 4" substrate, both without a barrier layer. The mean curvature is much lower in larger (and thicker) substrates. Results are not directly relevant for the study but confirm the validation of the set-up, initial curvature data and yield stresses.

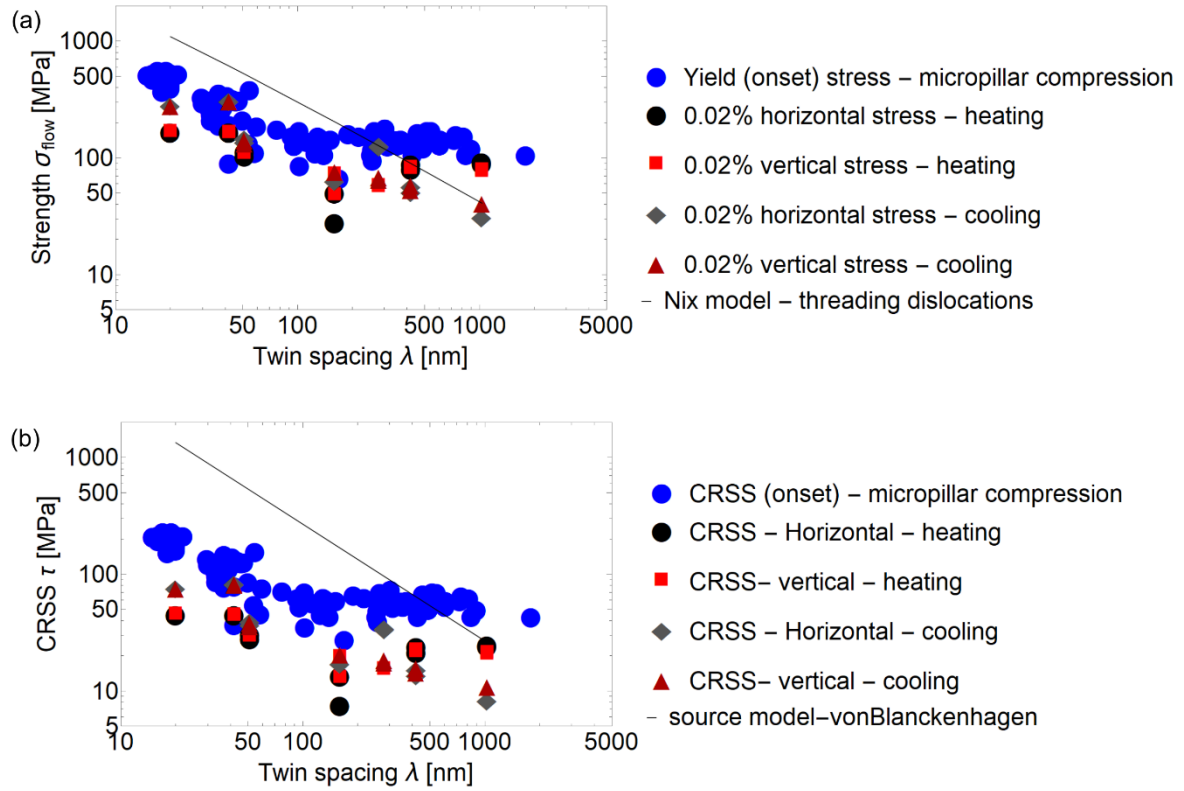


Fig. S2: (a) Variation of yield (onset) strength and corresponding (b) resolved shear stress for varying twin spacing λ in the present study compared with micropillar compression tests on similar samples [25] and theoretical thin film models [1, 16].

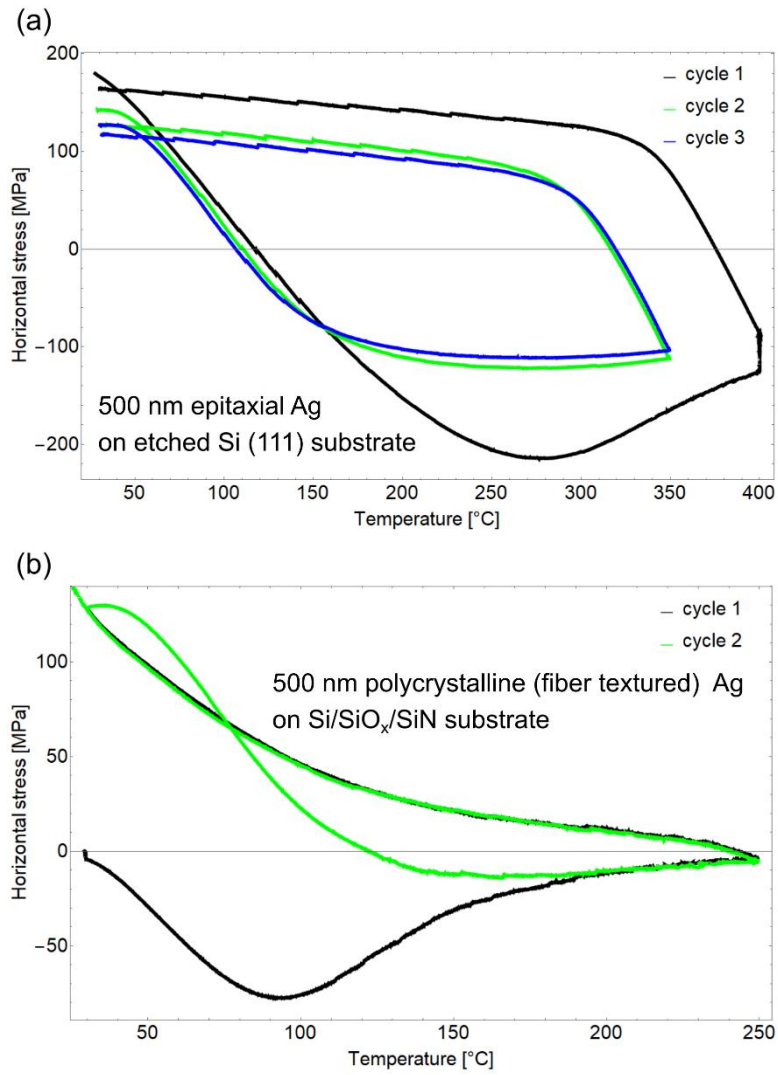


Fig S3: Thermomechanical deformation of a 500 nm (a) epitaxial nanotwinned Ag on etched Si(111) showing elastic – ideal plastic deformation due to dislocation plasticity and (b) polycrystalline $\langle 111 \rangle$ fiber textured Ag thin film on Si/SiN showing stress relaxation during first heating cycle due to diffusional creep.